ATMOSPHERIC SCIENCE

Ice core evidence for atmospheric oxygen decline since the Mid-Pleistocene transition

Yuzhen Yan[1,2]*, Edward J. Brook[3], Andrei V. Kurbatov[4], Jeffrey P. Severinghaus[5], John A. Higgins[1]

The history of atmospheric oxygen (PO_2) and the processes that act to regulate it remain enigmatic because of difficulties in quantitative reconstructions using indirect proxies. Here, we extend the ice-core record of PO_2 using 1.5-million-year-old (Ma) discontinuous ice samples drilled from Allan Hills Blue Ice Area, East Antarctica. No statistically significant difference exists in PO_2 between samples at 1.5 Ma and 810 thousand years (ka), suggesting that the Late-Pleistocene imbalance in O_2 sources and sinks began around the time of the transition from 40- to 100-ka glacial cycles in the Mid-Pleistocene between ~1.2 Ma and 700 ka. The absence of a coeval secular increase in atmospheric CO_2 over the past ~1 Ma requires negative feedback mechanisms such as P_{CO_2}-dependent silicate weathering. Fast processes must also act to suppress the immediate P_{CO_2} increase because of the imbalance in O_2 sinks over sources beginning in the Mid-Pleistocene.

INTRODUCTION

Oxygen (O_2) is an important life-supporting chemical species that plays a profound role in biological and geochemical processes on Earth. Past variations of O_2 partial pressure (PO_2) are commonly derived from geochemical models constrained by carbon and/or sulfur isotopes (*1*–*3*) and from proxies that are sensitive to the presence of oxygen, such as multiple sulfur isotopes (*4*), isotopes of redox-sensitive metals (*5*), iodine speciation (*6*), and the abundance of charcoal (*7*). The magnitude of the modeled or proxy-based PO_2 variations, however, often disagrees in both magnitude and sign (*8*), calling for more accurate reconstructions of the atmospheric O_2 concentration. Attempts to directly measure past PO_2 were limited to a few geologic archives that can preserve the atmosphere, such as amber (*9*) and fluid inclusions in minerals (*10*), although the robustness of these archives has been questioned (*11*).

Ice cores offer a unique opportunity to study past variations of PO_2 because the ice directly traps the ancient atmosphere. This distinctive capability motivated early measurements of molecular oxygen in the trapped air (*12*, *13*). However, the gas-trapping process in ice leads to a small exclusion of O_2 that has traditionally hindered the use of trapped O_2 in ice cores to derive true atmospheric PO_2, as the magnitude of this exclusion is comparable to that of the long-term PO_2 change (see Supplementary Text for a more in-depth review). For example, Landais *et al.* (*14*) first observed in the trapped air of Dome C (EDC) ice cores a decline of the O_2/N_2 ratios (expressed as $\delta O_2/N_2$ hereafter; $\delta = R_{sample}/R_{standard} - 1$, where R is the elemental or isotopic ratio of interest and the standard is modern air) over the past 800 thousand years (ka), but the authors did not provide a conclusive explanation on the origin of this decline (i.e., a natural long-term $\delta O_2/N_2$ trend versus a storage artifact).

Additional data from three more deep polar ice cores (GISP2, Vostok, and Dome F) also exhibit a persistent decreasing trend in $\delta O_2/N_2$, the magnitude of which is −8.4 ± 0.2‰/million year (Ma) (1σ) (*8*). This trend has recently been corroborated by additional measurements on better preserved cores from EDC (*15*), indicating that the Late-Pleistocene $\delta O_2/N_2$ decline is not an artifact but a robust atmospheric signal (*8*). Because the atmospheric reservoir of N_2 is expected to remain stable on time scales of hundreds of millions of years (*16*), the decline in ice core $\delta O_2/N_2$ is interpreted to reflect a decreasing PO_2. Proposed drivers of this decline, as presented by Stolper *et al.* (*8*), include net oxidation of reduced carbon and sulfur associated with enhanced Pleistocene physical and chemical weathering (*17*) and/or the effects of decreased ocean temperature on organic carbon burial rates (*3*). The exposure of continental shelves during glacial sea-level lowstands has recently been identified as another potential candidate (*18*).

Here, we extend the ice-core record of atmospheric PO_2 to ~1.5 Ma using "snapshots" of $\delta O_2/N_2$ in the air trapped in the glacial ice from the Allan Hills Blue Ice Area (BIA). The data include samples first reported by Yan *et al.* (*19*) and additional analyses conducted for the present study. We use the term snapshots to highlight the discontinuous nature of the blue ice samples and contrast that with the $\delta O_2/N_2$ time series obtained from continuous ice records (*8*, *15*). In Allan Hills BIA, ancient (up to 2.7 Ma) ice is transported toward the surface by a combination of glacial flow guided by the underlying bedrock topography and strong katabatic winds (fig. S1) (*19*, *20*). An absolute chronology of the ice is developed using the deficit of ^{40}Ar compared to the modern atmosphere (termed $^{40}Ar_{atm}$ and calculated as $\delta^{40}Ar/^{38}Ar - \delta^{38}Ar/^{36}Ar$) (*19*, *21*). $\delta^{18}O$ of the trapped O_2 provides additional stratigraphic links between two ice cores (fig. S2). Each individual $\delta O_2/N_2$ sample was assigned the age of the closest $^{40}Ar_{atm}$ datum. Using this chronology, we divided samples into three distinct time bins: 1.5 Ma (± 0.1 Ma), 810 ka (± 100 ka), and 400 ka (± 70 ka). The numbers represent the average of $^{40}Ar_{atm}$ ages weighted by their respective analytical uncertainty, bracketed by ±95% confidence intervals (CIs). The samples within each age bin do not necessarily have the exact same age. Rather, they are binned together because their age difference cannot be resolved by the existing $^{40}Ar_{atm}$ dating method. This means that the true width of age distribution (data S1) is likely wider than the 95% CI shown in the brackets. This is to our advantage because integrating over longer time intervals filters out high-frequency variations in PO_2 while preserving the long-term trend. Binning age groups this way allows the age uncertainty

[1]Department of Geosciences, Princeton University, Princeton, NJ, USA. [2]Department of Earth, Environmental and Planetary Sciences, Rice University, Houston, TX, USA. [3]College of Earth, Ocean, and Atmospheric Sciences, Oregon State University, Corvallis, OR, USA. [4]Climate Change Institute, University of Maine, Orono, ME, USA. [5]Scripps Institution of Oceanography, University of California, San Diego, La Jolla, CA, USA.
*Corresponding author. Email: yuzhen.yan@rice.edu

to be more rigorously defined and the effect of dating uncertainties on the long-term PO_2 change to be quantified.

Reconstructing atmospheric PO_2 from measurements of $\delta O_2/N_2$ of trapped air in ice cores requires corrections for fractionation during firnification and post-coring gas losses (*13*, *22*, *23*). In the study of Stolper *et al.* (*8*), corrections were achieved by first removing the insolation cycles in the $\delta O_2/N_2$ time series by linear regression and then by applying a constant gas-loss correction to $\delta O_2/N_2$ so each ice core $\delta O_2/N_2$ time series arrives at 0 when time is extrapolated to present. However, in the case of blue ice records from Allan Hills BIA, the insolation signals and gas losses cannot be directly accounted for because the age is not well resolved. In addition, the possibility of imperfect preservation of the $\delta O_2/N_2$ variability in a discontinuous record like blue ice implies that simple descriptive statistics (mean and variance) of the snapshots could be biased toward periods with high accumulation rates/better sample preservation (*19*). To reduce these confounding factors, we take advantage of the argon-to-nitrogen ratios (expressed as $\delta Ar/N_2$, again with modern air as the standard) in the trapped gases and use $\delta Ar/N_2$ as a proxy for fractionation modulated by insolation during firnification and fractionation due to post-coring gas loss.

Ar and N_2 are fractionated during bubble close-off and gas loss in a fashion similar to O_2 and N_2 but different in magnitude, leading to the covariation between $\delta O_2/N_2$ and $\delta Ar/N_2$ in ice cores (*13*, *22*, *23*). Part of this covariation arises from bubble close-off fractionation and is ultimately modulated by local insolation (*24*). As a result, correcting $\delta O_2/N_2$ using $\delta Ar/N_2$ measurements effectively removes the effect of local insolation on $\delta O_2/N_2$ during firnification. In the Supplementary Text, we show that post-coring gas loss can also be empirically accounted for by $\delta Ar/N_2$ corrections, although two other aspects of the $\delta Ar/N_2$ correction merit consideration here. First, due to the very small outgassing rate of ^{40}Ar (0.066‰/Ma) (*21*) and the long residence time of N_2 (*16*), atmospheric $\delta Ar/N_2$ variations will be far smaller than the changes in $\delta O_2/N_2$ inferred from ice cores and can thus be neglected. The effect of global ocean temperature on the solubility of Ar and N_2 and atmospheric $\delta Ar/N_2$ values is also expected to be small (<0.2‰) and can also be neglected. Second, this method is expected to be robust to the partial preservation and recovery of the true range of $\delta O_2/N_2$ or $\delta Ar/N_2$ variability, as long as the slope of the $\delta O_2/N_2$-$\delta Ar/N_2$ data remains the same (Fig. 1). In this case, the offset in two populations of $\delta O_2/N_2$-$\delta Ar/N_2$ is interpreted to reflect changes in PO_2.

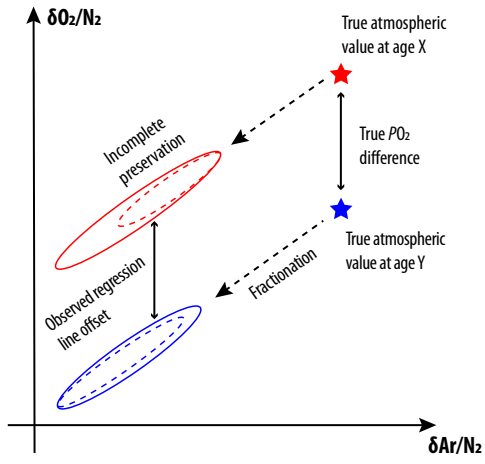

Fig. 1. A schematic illustration of paired $\delta O_2/N_2$-$\delta Ar/N_2$ approach (not to scale). Suppose there are two populations of $\delta O_2/N_2$-$\delta Ar/N_2$ data with different ages (stars), different magnitude of gas fractionation (dashed arrows), and different degree of sample preservation (dashed circles). The true atmospheric $\delta O_2/N_2$ changes can be inferred from the offset in the observed $\delta O_2/N_2$-$\delta Ar/N_2$ data if (i) the slopes of $\delta O_2/N_2$ against $\delta Ar/N_2$ within the two populations are the same and (ii) there is no secular change in $\delta Ar/N_2$. The first assumption is supported by the empirical observation that the $\delta O_2/N_2$-$\delta Ar/N_2$ slopes exhibited in Allan Hills samples are statistically indistinguishable among three intervals. The second assumption is supported by a lack of long-term ice core $\delta Ar/N_2$ trend over the past 800 ka (*8*).

RESULTS

Testing the paired $\delta O_2/N_2$-$\delta Ar/N_2$ approach using EDC and Vostok ice

To test the validity of this paired $\delta O_2/N_2$-$\delta Ar/N_2$ approach, we first used a recently published, gravitationally corrected dataset of $\delta Ar/N_2$ from EDC ($N = 40$) between 120 and 700 ka to correct the $\delta O_2/N_2$ data measured from the same ice (*25*). This dataset was obtained from ice stored at −50°C and is considered free from post-coring gas-loss fractionation. Six age bins were identified. In each age bin, $\delta Ar/N_2$ was normalized to −6.3‰, the average value of all $\delta Ar/N_2$ data in the record, to calculate $\delta O_2/N_2$ using the observed $\delta O_2/N_2$-$\delta Ar/N_2$ relationship in that bin (fig. S3). Except in the youngest (135 ka) group, the corrected $\delta O_2/N_2$ falls almost exactly on the trend line of $\delta O_2/N_2$ versus time [−7.0 ± 0.6 (1σ) ‰/Ma; Fig. 2] calculated from a high-resolution Dome C $\delta O_2/N_2$ record ($N = 325$) compiled by Extier *et al.* (*15*). Note that this high-resolution Dome C $\delta O_2/N_2$ record does not include the low-resolution $\delta O_2/N_2$ time series. The trend line observed in the low-resolution $\delta O_2/N_2$ record after $\delta Ar/N_2$ corrections is −9.1 ± 2.5‰/Ma (1σ). In spite of the relatively low temporal resolution of the data measured by Haeberli *et al.* (*25*), the $\delta Ar/N_2$ correction manages to reproduce the trend in $\delta O_2/N_2$, highlighting that this approach does not require the full or unbiased preservation of the true $\delta O_2/N_2$ and $\delta Ar/N_2$ variability in the ice.

Next, we applied the paired $\delta O_2/N_2$-$\delta Ar/N_2$ approach to the Vostok $\delta O_2/N_2$ record between 243.5 and 372.5 ka (*8*, *24*), which exhibits a temporal trend of −20.2 ± 3.3‰/Ma (1σ; fig. S4). We note that the trend in Vostok is steeper and with larger uncertainties than the rate inferred from the Dome C $\delta O_2/N_2$ record, possibly because of Vostok record's relatively short time span (~130 ka) and hence a relatively large insolation signal here. We arbitrarily divided the Vostok gas data into two age groups: 243.5 to 300 ka ($N = 27$) and 300 to 372.5 ka ($N = 29$). When $\delta Ar/N_2$ is normalized to −4.8‰, the average value of all Vostok $\delta Ar/N_2$ data between 243.5 and 372.5 ka, the estimated $\delta O_2/N_2$ (± 2σ) is −8.9 ± 0.6‰ in the >300-ka group and −10.6 ± 0.5‰ in the <300-ka group. Using a time span of 64.5 ka (the difference between 271.75 and 336.25 ka), the inferred $\delta O_2/N_2$ rate of change is −26.0 ± 6.2‰/Ma (1σ). The $\delta Ar/N_2$ correction leads to about two times larger uncertainty for the final estimated $\delta O_2/N_2$ change rate, possibly due to the scatters in the $\delta O_2/N_2$ and $\delta Ar/N_2$ cross-plot. Another reason may be the short time span and the small magnitude of the change (hence the larger relative error).

To sum up, in both cases of EDC and Vostok ice, corrections by $\delta Ar/N_2$ are able to recover a rate of $\delta O_2/N_2$ change that is statistically indistinguishable from the rate of $\delta O_2/N_2$ changes regressed directly against time. This agreement justifies the application of paired $\delta O_2/N_2$-$\delta Ar/N_2$ approach in 1.5-Ma samples from the Allan Hills BIA.

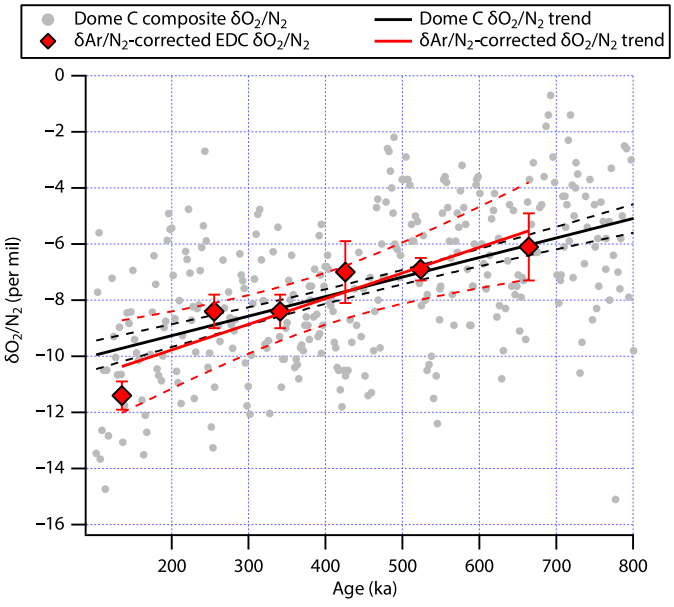

Fig. 2. Testing the paired $\delta O_2/N_2$-$\delta Ar/N_2$ using the Dome C ice core gas records. A composite Dome C $\delta O_2/N_2$ (gray dots) compiled by Extier *et al.* (*15*) yields a temporal trend of −7.0 ± 0.6‰/Ma (1σ; shown as a solid line bracket by two dashed curves). The corrected $\delta O_2/N_2$ data (red squares with error bars representing the 95% CI) binned into six age groups (fig. S3) also yield a decreasing trend with a slope of −9.1 ± 2.7‰/Ma (1σ). Raw $\delta O_2/N_2$ and $\delta Ar/N_2$ data for correction are from Haeberli *et al.* (*25*).

Table 1. Results of ordinary least squares linear regression of $\delta O_2/N_2$ against $\delta Ar/N_2$ measured in Allan Hills ice core samples. Errors are given as 95% CIs.

	Post-MPT (400 ± 70 ka)	MPT (810 ± 100 ka)	Pre-MPT (1.5 ± 0.1 Ma)
Slope	1.74 ± 0.44	1.60 ± 0.50	1.51 ± 0.38
Y intercept	−0.9 ± 3.1‰	2.2 ± 3.8‰	2.0 ± 2.9‰
Correlation coefficient *r*	0.84	0.76	0.86
Corrected $\delta O_2/N_2$ (when $\delta Ar/N2 = -7.1‰$)	−13.3 ± 1.2‰	−9.2 ± 0.8‰	−8.7 ± 0.8‰

$\delta O_2/N_2$-$\delta Ar/N_2$ in Allan Hills ice samples

$\delta O_2/N_2$ and $\delta Ar/N_2$ measured on Allan Hills ice samples and corrected for gravitational fractionation using the $\delta^{15}N$ of N_2 (*26*) are also linearly correlated (Fig. 3). In addition, we find that the slope of the regression line in the three age units is statistically indistinguishable (Table 1). This lack of difference suggests that there has been no fundamental change to the physical mechanisms that fractionate O_2, Ar, and N_2 over time in the Allan Hills ice, and provides an empirical justification for the use of $\delta Ar/N_2$ to correct Allan Hills $\delta O_2/N_2$ data for fractionation associated with bubble close-off and gas losses, and incomplete sampling of $\delta O_2/N_2$ variability associated with local insolation. Given the small difference in the slope of $\delta O_2/N_2$ against $\delta Ar/N_2$ across the three age units, we first normalize $\delta O_2/N_2$ values by correcting measured $\delta Ar/N_2$ value to −7.1‰, the average value of all $\delta Ar/N_2$ data (N = 88) reported in this study. Physically, this normalization means that the effect of insolation on $\delta O_2/N_2$ has been removed, and all the $\delta O_2/N_2$ data have the same extent of gas loss. This is different from normalizing $\delta Ar/N_2$ to 0, which would effectively eliminate all gas losses. Next, we applied a secondary gas loss correction by adding 17.4‰ to the estimated $\delta O_2/N_2$ to obtain atmospheric $\delta O_2/N_2$, conceptually similar to that by Stolper *et al.* (*8*). $\delta O_2/N_2$ should reach 0 when time is extrapolated to the present day (Fig. 4). This secondary correction does not change the slope inferred from the estimated $\delta O_2/N_2$ after $\delta Ar/N_2$ normalization. Extrapolating $\delta Ar/N_2$ to 0 (the theoretical true atmospheric value) for $\delta O_2/N_2$ correction does not change our results but is associated with larger uncertainties (see *y* intercepts in Table 1).

When normalized to the mean $\delta Ar/N_2$ value (−7.1‰), the corrected $\delta O_2/N_2$ is −8.7 ± 0.8‰ (95% CI; N = 25) in the 1.5 ± 0.1 Ma ice, −9.2 ± 0.8‰ (95% CI; N = 34) in the 810 ± 100 ka ice, and −13.3 ± 1.2‰ (95% CI; N = 29) in the 400 ± 70 ka ice (Table 1). The inferred rate of Late-Pleistocene $\delta O_2/N_2$ change, calculated by dividing the $\delta O_2/N_2$ difference in the 810 ± 100 ka and 400 ± 70 ka ice by their age difference, is −10.2 ± 2.5‰/Ma (1σ). The uncertainty is estimated by a Monte-Carlo simulation in which the division operations are repeated 10,000 times assuming a normal distribution for $\delta O_2/N_2$ and age according to their calculated 95% CIs. The uncertainty in our estimates is relatively large because our approach has fewer samples than the continuous $\delta O_2/N_2$ records obtained from deep ice cores and the $^{40}Ar_{atm}$ ages of the blue ice introduce another layer of uncertainty. Nevertheless, the change in PO_2 estimated from Allan Hills ice is statistically indistinguishable from the estimated change of −8.4 ± 0.2‰/Ma (1σ) diagnosed by Stolper *et al.* (*8*), supporting our paired $\delta O_2/N_2$-$\delta Ar/N_2$ approach.

In contrast, the calculated rate of PO_2 change between the $\delta O_2/N_2$-$\delta Ar/N_2$ dataset recorded in the 1.5-Ma and 810-ka ice is −0.7 ± 0.9‰/Ma (1σ), statistically indistinguishable from zero. Because of the large size of the atmospheric O_2 reservoir (3.8×10^{19} mol) and the relatively small O_2 flux associated with geologic sources and sinks, the geologic residence time of atmospheric O_2 is over 1 Ma (*27*), meaning that large PO_2 fluctuations between 1.5 Ma and 810 ka unlikely result from geologic O_2 sources or sinks. Some readers may identify photosynthesis and aerobic respiration in the biological cycling of oxygen as sources and sinks of O_2, but the biosphere reservoir of organic carbon is two orders of magnitude smaller than the atmospheric O_2 reservoir (fig. S5). For example, glacial-interglacial changes of terrestrial biosphere carbon reservoir size amount to ~3 to 7×10^{16} mol O_2 (*28*), which would lead to a shift of the PO_2 of ~1 to 2‰. To illustrate this point further, permafrost is a major source of unstable organic carbon reservoir and represents ~1×10^{18} g carbon in Earth's near surface (0 to 3 m) (*29*). Oxidizing this entire surface reservoir would only lead to a 2‰ decline in atmospheric O_2. We thus conclude that the initiation of the decline in atmospheric PO_2 approximately coincided with the Mid-Pleistocene transition (MPT), a period between ~1250 and 700 ka where Earth's climate underwent a fundamental shift characterized by the emergence of high-amplitude glacial-interglacial oscillations and an increase in the duration of glacial cycles from 40 to 100 ka (*30*–*32*).

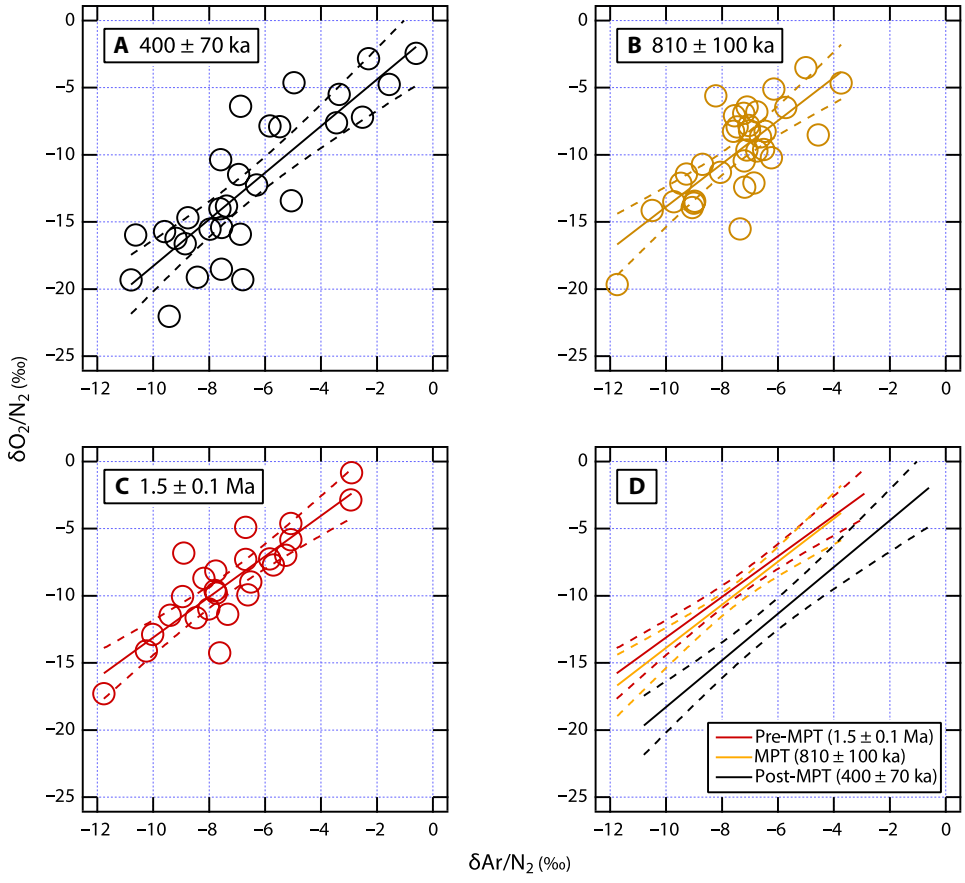

Fig. 3. Cross-plot of $\delta O_2/N_2$ versus $\delta Ar/N_2$ measured in Allan Hills ice core samples, binned according to their age (error represents the 95% CI of the regression slopes). Solid lines in (**A**) to (**C**) represent the regression lines of $\delta O_2/N_2$ against $\delta Ar/N_2$, with the CI bracketed by the dashed lines. The regression lines of the three intervals are shown in (**D**) to demonstrate their offset.

DISCUSSION

Assuming a geologic residence time of ~2 Ma (*27*), the decline in $\delta O_2/N_2$ over the last 800 ka is equivalent to a ~2% excess of O_2 sinks over sources (*8*). These O_2 sources and sinks include (i) the burial of reduced carbon, sulfur, and iron species into the sedimentary reservoir (geologic O_2 source) and (ii) the oxidative weathering of the previously buried reduced carbon, sulfur, and iron species exhumed to Earth's surface (geologic O_2 sink). Because the total amount of O_2 consumed over the last 800 ka (~2.4×10^{17} mol) is equivalent to ~1.2 times the combined size of the terrestrial and marine biosphere and soils (in O_2 equivalents; fig. S5), changes in geologic sources and/or sinks must act to drive the long-term PO_2 change.

Our new data, which almost doubles the length of the existing ice-core record of atmospheric O_2 (*8*), indicates (i) an even slower rate of change of PO_2 on a multimillion-year time scale and (ii) that the decline over the last 800 ka appears to have begun sometime around the MPT (Fig. 4). Before this, sources and sinks of O_2 appear to have been in close balance. That the MPT marks the beginning of this small Late-Pleistocene imbalance in O_2 sources and sinks is important for two reasons. First, the timing suggests a causal link between the MPT and a change in the global O_2 balance favoring sinks over sources. This link, regardless of its ultimate cause(s), provides unique information about the processes that regulate atmospheric O_2 on geologic time scales. Second, assuming that the global CO_2 and O_2 cycles are linked, P_{CO_2} (partial pressure of CO_2) should begin to increase as soon as PO_2 starts to decline. However, there is no apparent increase in atmospheric CO_2 across the MPT (Fig. 4), which requires mechanisms to stabilize atmospheric P_{CO_2}.

Across the MPT, the increase of global ice volume added up to ~60 m in sea-level equivalents, estimated from changes in benthic foraminiferal $\delta^{18}O$ values (*30*, *33*, *34*). This volumetric increase appears to have been accommodated largely by an increase in ice sheet thickness, as geologic evidence indicates that the areal extent of Laurentide Ice Sheet has been similar since Early Pleistocene (*35*). In the meantime, mountain glaciers appear to have expanded considerably across the MPT in the Alps, Canadian Rockies, Tibetan Plateau, and Patagonia [(*36*) and references therein]. Deep-sea temperature changes across the MPT reconstructed from Mg/Ca ratios recorded in foraminiferal shells are ambiguous and inconclusive due to different regional trends (*33*, *37*). An alternate approach, which subtracts an independently reconstructed global ice-volume from the benthic $\delta^{18}O$ stack, shows that there appears to be no substantial deep-sea cooling across the MPT (*34*). Interglacial CO_2 levels remained somewhat stable before and after the MPT varying between 260 and 300 parts per million (ppm), but a decrease of glacial CO_2 concentration minima by ~30 ppm (Fig. 4) was reconstructed from blue ice (*19*) and from boron isotopes in marine fossils (*38*).

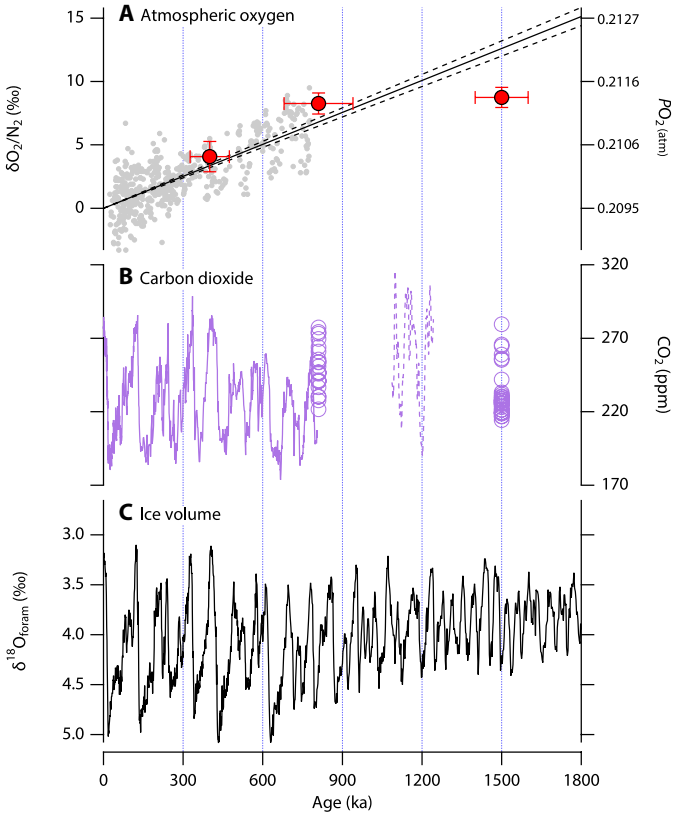

Fig. 4. Pleistocene $\delta O_2/N_2$, P_{CO_2}, and ice volume. (**A**) An ice core–based time series of atmospheric $\delta O_2/N_2$ composite (gray circles) (*8*) and discontinuous atmospheric $\delta O_2/N_2$ snapshots reconstructed from blue ice $\delta O_2/N_2$ (red circles, this work). Black line represents the extrapolated regression line of the continuous 800-ka $\delta O_2/N_2$ composite, with the 95% CIs bracketed by the two dashed lines. Vertical error bars associated with blue ice $\delta O_2/N_2$ are the 95% CIs of the corrected $\delta O_2/N_2$ when $\delta Ar/N_2$ is normalized to −7.1‰. Horizontal error bars represent the 95% CI of the age estimates. The blue ice $\delta O_2/N_2$ values were systematically increased by 17.4‰, so $\delta O_2/N_2$ reaches 0 when extrapolated from the 810- and 400-ka data to present, consistent with the treatment of the composite atmospheric $\delta O_2/N_2$ time series (*8*). (**B**) A continuous ice core CO_2 record over 800 ka (solid purple line) (*64*–*67*), atmospheric CO_2 reconstructions based on boron isotopes (dashed purple line) (*38*), and the Allan Hills blue ice CO_2 data, grouped to the same age assignment as for $\delta O_2/N_2$ (purple circles) (*7*, *32*). (**C**) Stacked oxygen isotope composition of benthic foraminifera (LR04) (*30*).

Existing hypotheses on the Late-Pleistocene decline of O_2 include (i) a decrease in the burial of reduced carbon and sulfur species linked to long-term ocean cooling and an increase in the solubility of O_2 in the seawater [a hypothesis first put forward by Shackleton (*3*) to explain the Cenozoic history of O_2], (ii) an increase in the oxidation of reduced carbon and sulfur species associated with lower sea-level during glacial maxima and the exposure of recently deposited marine sediments (*18*), and/or (iii) an increase in the oxidation of reduced carbon and sulfur species relative to enhanced organic carbon and pyrite burial due to higher erosion rates (*8*).

Ocean cooling over the Pleistocene [hypothesis (i)] is possible, although it is not firmly established from global deep-sea temperature records (*33*, *34*) or marginal marine environments where most of the reduced carbon and sulfur is buried. In contrast, increased oxidation of reduced carbon and sulfur associated with increased exposure of the continental shelf during the sea-level lowstands of the Late Pleistocene [hypothesis (ii)] can explain ~70% of the Late-Pleistocene PO_2 decline (*18*). However, this estimate is likely an upper limit, because the calculation is based on pyrite exposed by a ~90-m sea-level difference in the Late-Pleistocene glacial cycles. If we apply the same mechanism given the glacial-interglacial sea-level difference of ~60 m before the MPT, either PO_2 declined at a slower rate of −4‰ to −5‰/Ma in the Early Pleistocene (not consistent with observation) or only the deeper pyrite newly exposed by the additional 30-m sea-level drop after the MPT acted to break the balance between oxygen sources and sinks. In the latter case, the expected effect of continental shelf pyrite exposure and oxidation will only be able to account for ~21% of the observed Late-Pleistocene atmospheric O_2 decline.

Increased oxidation of reduced carbon and sulfur associated with increased Late-Pleistocene continental glaciation and erosion [hypothesis (iii)] is therefore more likely to have contributed to the post-MPT $\delta O_2/N_2$ decline. For example, a link between more extensive post-MPT mountain glaciation and an increase in erosion rates is observed at St. Elias Mountains, Alaska (*39*). In addition, glacial weathering elevates pyrite oxidation that acts as a net O_2 sink (*40*) and increases the oxidation rates of fossil organic carbon in rocks by a factor of 2 to 3 in glaciated mountainous regions due to enhanced frost cracking, abrasion, oxygen availability in deeper soil horizons, and microbial activity (*41*). All these glaciation-facilitated processes could enhance O_2 sinks, thereby leading to a PO_2 drawdown since the MPT with the presence of larger ice sheets. We note that increasing erosion rates also promote organic and pyrite burial, and the net effect on PO_2 remains not fully resolved (*42*). In any case, both hypotheses (ii) and (iii) suggest that the MPT could not only reshape the glacial-interglacial cycles but also profoundly affect the biogeochemical cycles of carbon and oxygen.

Last, a decline in PO_2 due to changes in organic carbon burial and oxidation would inject CO_2 to the coupled atmosphere-ocean system. Even if that decline is entirely due to the enhanced pyrite oxidation, atmospheric CO_2 would still increase—albeit with a smaller magnitude due to interactions with the inorganic carbon cycle. When coupled with calcium carbonate dissolution, pyrite oxidation has a stoichiometric 8:15 ratio of CO_2 produced to O_2 consumed (*18*). This is approximately half the yield of CO_2 during oxidation of organic carbon, assuming the composition of the organic carbon is CH_2O (i.e., 1 mol of CO_2 is produced when 1 mol of O_2 is consumed). Only when all the H^+ produced during pyrite oxidation is consumed by silicate dissolution can P_{CO_2} be truly decoupled from the oxygen cycle (*40*).

Records of atmospheric CO_2 from both ice cores (*19*) and boron isotopes in foraminifera (*38*) indicate that average CO_2 levels either did not substantially change or actually declined across the MPT (Fig. 4). As noted by Stolper *et al.* (*8*), this observation can be explained by the P_{CO_2}-dependent silicate weathering feedback with a 200- to 500-ka response time. However, we note that with even the fastest response times P_{CO_2} must still increase in order for the feedback to establish a balance between sources and sinks [figure 3 in the study of Stolper *et al.* (*8*)]. This instantaneous increase in P_{CO_2} was ignored by Stolper *et al.* (*8*) because it only occurs following the initiation of a decline in PO_2 and the timing of that initiation was not resolved in the 800-ka PO_2 record. Our ability to identify the MPT as the initiation of a decline in PO_2 means that this initial increase in CO_2 can no longer be ignored. Additional responses and/or enhanced

feedbacks within the global carbon cycle are required to explain why CO_2 remained constant or declined across the MPT. Although speculative, two promising candidates are (i) enhanced CO_2 storage in the deep Atlantic Ocean (*43*) enabled by seafloor calcium carbonate dissolution (*44*) and linked to ocean circulation changes (*45*) and (ii) enhanced chemical weathering resulting from the transition from regolith to fresh, unweathered crystalline bedrock beneath the Laurentide Ice Sheet that became first exposed around the MPT (*31*).

Oxygen-to-nitrogen ratios in the air bubbles trapped in blue ice from Allan Hills, East Antarctica provide a record of atmospheric O_2 extending to the Early Pleistocene after correction by argon-to-nitrogen ratios preserved in the same sample. This correction approach is tested on the Vostok and Dome C $\delta O_2/N_2$ records and successfully reproduces their long-term trends. A decline in PO_2 inferred from 810- and 400-ka Allan Hills ice samples agrees with PO_2 reconstructions based on continuous ice records (*8*, *15*), further supporting the $\delta Ar/N_2$ correction method. There is no statistically significant $\delta O_2/N_2$ difference between samples at 1.5 Ma and 810 ka, suggesting a stable mean O_2 level and a balanced O_2 sources and sinks before the MPT. The coincidence of PO_2 decline with the MPT hints at the role of glaciation that enhances erosion rates as well as promotes the oxidative weathering of sedimentary organic carbon and reduced sulfur species. The lack of transient P_{CO_2} increase in response to the declining PO_2 requires responses in the carbon cycle to stabilize atmospheric CO_2, possibly first via a fast increase of deep ocean carbon storage as a result of ocean circulation changes (*43*, *45*) and in the long term by an enhanced silicate weathering due to the exposure of pre-Cambrian crystalline bedrock underneath the Laurentide Ice Sheet starting around the MPT (*31*).

MATERIALS AND METHODS

Glaciological settings

Allan Hills (76.73°S, 159.36°E) is located ~100 km to the northwest of the McMurdo Dry Valleys in Victoria Land, East Antarctica. Sampling sites are located to the west of the Allan Hills nunatak in the Main Ice Field (MIF; fig. S1). Samples reported in this study come from two boreholes in the MIF with close proximity: ALHIC1502 (76.73286°S, 159.35507°E) and ALHIC1503 (76.73243°S, 159.35620°E). Local glaciological conditions in the MIF are documented elsewhere (*46*–*48*), and Dadic *et al.* (*49*) provide a detailed survey of meteorological conditions and surface snow properties. In brief, the Allan Hills area is characterized by constant katabatic wind, sweeping away shallow snow patches and ablating the ice at the surface (*48*). The presence of blue ice near Allan Hills is further facilitated by a nunatak obstructing the upcoming glacial flow and a steep slope on the lee side of a mountain buried under the ice (*20*, *50*). The steep bedrock slope and low basal temperature inhibit glacial flow, thereby promoting the preservation of exceptionally old ice. Although modern-day glaciological survey reveals a local accumulation regime (*51*), the source region of the ice buried at depth in the Allan Hills BIAs remains unclear.

While the glaciological conditions favor the preservation of old ice here, they also pose several challenges to using blue ice as paleoclimate archives. First, the unique glaciological dynamics at the BIAs make it difficult to constrain the chronology of the ice, as ice movement has likely disturbed the otherwise continuous ice stratigraphy. If the age of the blue ice samples is within 800 ka, they could be synchronized to the deep ice cores via various age markers (*52*). However, if the age exceeds 800 ka, which is the case of Allan Hills blue ice, there is no existing record to synchronize to. An absolute dating method that does not require prior glaciological information is needed. In the section below, we describe the time scale development using gravitationally corrected $^{40}Ar/^{38}Ar$ ratio ($^{40}Ar_{atm}$).

Time scale development

We established the blue ice chronology by measuring the gravitationally corrected $^{40}Ar/^{38}Ar$ ratios ($^{40}Ar_{atm}$, calculated as $\delta^{40}Ar/^{38}Ar - \delta^{38}Ar/^{36}Ar$) in the trapped gases (*21*). Individual $^{40}Ar_{atm}$ datum and the corresponding uncertainty is included in data S1. This method takes advantage of the fact that atmospheric ^{40}Ar burden slowly increases over time because of the radioactive decay of ^{40}K in the solid Earth, while ^{38}Ar and ^{36}Ar are primordial and their abundance is stable over geologic history. The rate of $^{40}Ar_{atm}$ change is +0.066‰/Ma over the past 800 ka (*21*), and we caution that the outgassing rate could have changed before the MPT and therefore changed our extrapolation results. If weathering rates have increased since the MPT due to more extensive glaciation, the outgassing rate of ^{40}Ar is expected to be lower in the Early Pleistocene than in the Late Pleistocene. In this scenario, the >800-ka samples discovered at the Allan Hills BIA would have an even older age. This age underestimation means that the 1.5-Ma data point in Fig. 4 would need to be moved to the right, but the conclusions of this study would remain the same because $\delta O_2/N_2$ is essentially constant between the 810-ka and 1.5-Ma age bins.

In addition, because the depths of $\delta O_2/N_2$ samples are different from those of $^{40}Ar_{atm}$ samples, in most cases, the age of $\delta O_2/N_2$ samples was assigned to their closest $^{40}Ar_{atm}$ datum reported by Higgins *et al.* (*53*) and Yan *et al.* (*19*). Note that the analytical uncertainties associated with the $^{40}Ar_{atm}$ measurements (at least 10% of the sample age) preclude an age assignment precise enough to establish a time series. To maximize the utility of the $^{40}Ar_{atm}$ data, we classify samples into different age groups and calculate the average age ($\hat{\mu}$) on the basis of individual $^{40}Ar_{atm}$ measurements (x_i), weighted by their corresponding uncertainty (σ_i)

$$\hat{\mu} = \frac{\Sigma x_i/\sigma_i^2}{\Sigma 1/\sigma_i^2} \quad (1)$$

The error associated with the weighted mean is given by

$$\sigma^2(\hat{\mu}) = \frac{1}{\Sigma 1/\sigma_i^2} \quad (2)$$

Underlying this error estimation is the implicit assumption that all samples within the age bin have the exact same age and the precision of age estimates is purely limited by the analytical precision of $^{40}Ar_{atm}$. We acknowledge that there is no independent evidence to support this assumption. That being said, the purpose of such age binning is to provide a quantifiable age uncertainty that can then be taken into consideration in calculating long-term PO_2 trend. Basing these calculations on the difference between the average age of two or more intervals has proven valid in EDC (fig. S3) and Vostok (fig. S4). In any case, uncertainties associated with age will affect the estimated rate of PO_2 decline in the Late-Pleistocene, but will not change the conclusion of a stable atmospheric O_2 level before the MPT.

Three age groups were identified and listed in Table 1: pre-MPT, MPT, and post-MPT, in accordance with the definition by Yan *et al.* (*19*). The post-MPT group has an average $^{40}Ar_{atm}$ of 400 ± 70 ka

(95% CI) from 23 $^{40}Ar_{atm}$ measurements made on 20 depths in ALHIC1502 and ALHIC1503 cores. Similarly, the mean age of the MPT group is calculated to be 810 ± 100 ka (95% CI), constrained by nine $^{40}Ar_{atm}$ data points from six depths. The pre-MPT age group has three sub-age units: 1.5, 2.0, and 2.7 Ma. In this study, we only include samples in the 1.5-Ma subgroup, the reason of which is discussed in the "Data quality and rejection criteria" section. This age (1.5 ± 0.1 Ma; 2σ) is estimated by four unreplicated $^{40}Ar_{atm}$.

In the upper 170 m of ALHIC1502, there are only four $^{40}Ar_{atm}$ data that provide age constraints. The transition from post-MPT to MPT age unit in ALHIC1502 is located between 143.19 and 172 m, the last post-MPT and the first MPT $^{40}Ar_{atm}$-based age estimates, respectively. This data gap requires alternative estimates to identify the transition from post-MPT to MPT ice samples. By comparison, the chronology of ALHIC1503 is better constrained by 33 $^{40}Ar_{atm}$ analyses from 27 depths. We assume that ALHIC1502 and ALHIC1503 have an overall similar age-depth structure given their close proximity, and the variations in $\delta^{18}O_{atm}$ can be used as a marker to identify the depth at which MPT ice first appears in ALHIC1502. In ALHIC1503, the transition from post-MPT to MPT age unit occurs along with a rapid $\delta^{18}O_{atm}$ decline from 1.361 to 0.488‰ (*53*). In ALHIC1502, this transition occurs between 146.40 and 147.99 m (fig. S2 and data S2). We therefore choose the midpoint in between (147.20 m) as the arbitrary divide between post-MPT and MPT ice. Note that there are no $\delta O_2/N_2$ data points between 146.40 and 147.99 m in ALHIC1502, so the conclusion of this paper is not affected by where this divide is exactly chosen.

Another interesting feature of the depth profile of $^{40}Ar_{atm}$ in ALHIC1502 is the rather young (~880 ka) age in the deepest measured sample with a depth of 190 m. In contrast, the deepest $^{40}A_{ratm}$ measurement in ALHIC1503 yields an age of 2.7 ± 0.3 (1σ) Ma. There are two possible explanations: (i) The ice dates back to the MPT and is buried under the pre-MPT ice due to stratigraphic disturbance or (ii) the age is underestimated because of input of radiogenic ^{40}Ar from the bedrock. We have no way of identifying the true cause(s), but either way, it would not affect the conclusion of this paper because the $\delta O_2/N_2$ data were rejected on other bases (see the "Data quality and rejection criteria" section).

Analytical methods for $\delta O_2/N_2$ and $\delta Ar/N_2$

The analytical procedures of $\delta O_2/N_2$, $\delta Ar/N_2$, and $\delta^{15}N$ of N_2 data reported in this study are modified from Dreyfus *et al.* (*54*) and described in detail by Yan *et al.* (*19*). A brief summary is outlined below. A total of ~20-g ice was cut from the core, with the outer 2 to 3 mm removed and subsequently melted under vacuum. To achieve that vacuum, the ambient air inside the glass container that carried the ice was pumped away for 3 min by a turbomolecular pump with the container placed in a dry ice–isopropanol bath. The ~200-ml glass container has a Louwers-Hapert valve at the top and an Ace-Thred connection sealed by a Viton O-Ring. After ice melted, the glass vial was loaded onto an electromechanical rotator to let the air and meltwater equilibrate (*55*). After 4 hours, the glass vial was taken down from the rotator, connected to a Büchner flask upside down, and drained by a rotatory pump. Then, the vial was flipped upside down and placed in a −30°C bath to let residual water refreeze. Gases in the headspace were cryogenically collected at 4 K in a stainless steel dip tube submerged in liquid helium. During the gas collection, H_2O and CO_2 were removed by two sequential gas traps, one kept at −100°C and the second placed in liquid nitrogen bath.

The dip tube was allowed to warm up at room temperature for at least an hour. Later, it was attached to an isotope-ratio mass spectrometer (Thermo Delta Plus XP) for elemental and isotopic analysis for ~30 min. The configuration of the mass spectrometer permits simultaneous measurement of mass 28 ($^{14}N^{14}N$) to mass 44 ($^{12}C^{16}O_2$), thereby yielding raw $^{15}N/^{14}N$, O_2/N_2, Ar/N_2, and $^{18}O/^{16}O$ ratios at the same time. Analysis of each single sample was made up of 24 individual cycles, each with a 16-s integration time. The raw $\delta^{15}N$, $\delta^{18}O$, $\delta O_2/N_2$, and $\delta Ar/N_2$ ratios were corrected for pressure imbalance based on the ion currents on the sample and reference sides (*12*). Pressure-corrected $\delta^{15}N$ and $\delta^{18}O$ were further corrected for the elemental composition of the O_2-N_2 mixture (termed "chemical slope correction") (*12*). After pressure imbalance and chemical slope corrections, pressure and chemically corrected $\delta^{15}N$ was used to correct for gravitational fractionation in $\delta O_2/N_2$, $\delta Ar/N_2$, and $\delta^{18}O$ of O_2 (termed $\delta^{18}O_{atm}$). Those gravitationally corrected data, presented in data S2, are used for interpreting atmospheric O_2 concentrations.

The final pooled SDs of all Allas Hills $\delta O_2/N_2$, $\delta Ar/N_2$, and $\delta^{18}O_{atm}$ [excluding those reported by Higgins *et al.* (*53*) because of their procedural differences] are ±3.372, ±2.081, and 0.027‰, respectively. All δ values have been standardized to the modern atmosphere. We note that the analytical uncertainties of Allan Hills $\delta O_2/N_2$ reported here, by Yan *et al.* (*19*), and by Higgins *et al.* (*53*) are worse than the reproducibility of the same properties achieved in other deep ice cores, which is well noted by Stolper *et al.* (*8*) and led to the exclusion of 1 Ma Allan Hills blue ice $\delta O_2/N_2$ data in that study. For example, the reproducibility of $\delta O_2/N_2$ measured on EDC and Dome Fuji ice samples is 0.37‰ (*15*) and 0.2‰ (*56*), respectively. This difference in reproducibility likely arises from the fact that gases are trapped in bubbles in the Allan Hills ice, whereas the EDC and Dome F $\delta O_2/N_2$ data were measured on ice that exclusively contains clathrate. Similar conclusions are drawn from Vostok samples, where gases contained in bubbles exhibit more scatter in measured $\delta O_2/N_2$ than gases from bubble-free, all-clathrate ice (*57*). It may be the case that bubbles are more susceptible to gas loss and fractionation as compared to clathrates. At any rate, the difference of bubbles versus clathrates means that Allan Hills data cannot be directly compared against other deep ice core data. Internal comparison between Allan Hills samples (all with bubbles only) of different ages is still justified. We acknowledge that the estimated $\delta O_2/N_2$-$\delta Ar/N_2$ slope and intercept derived from ice with bubbles must have larger uncertainty than does the slope and intercept derived from ice with clathrates only, but we expect the estimate to be unbiased, which is important for estimating long-term PO_2 changes.

Here, we quantitatively investigate how much the observed $\delta O_2/N_2$ reproducibility is limited by the analytical precision associated with mass spectrometer analyses, using the 25 samples (all with replication) dating back to 1.5 Ma as an example. With a pooled SD of ±3.372‰ (1σ), 25 unique samples each with replication should yield a 95% CI of ±0.95‰, if all the disagreements between the $\delta O_2/N_2$ replicate values arise from the mass spectrometer measurements. The calculation is as follows: The observed pooled SD (3.372‰) is first divided by the square root of 2 to take replicate analyses into account, then divided by the square root of 25, the number of unique samples, and finally multiplied by 2 to yield the 95% CI. However, the 95% CI of the $\delta O_2/N_2$-$\delta Ar/N_2$ regression line is ±0.79‰ at $\delta Ar/N_2$ = −7.1‰, less uncertain than what pure analytical uncertainties alone would dictate. This observation means that correction by $\delta Ar/N_2$ reduces the uncertainties in the $\delta O_2/N_2$ dataset. Thus, the

large analytical uncertainty of $\delta O_2/N_2$ measured on ice with bubbles must partly be sourced from processes that fractionate both $\delta O_2/N_2$ and $\delta Ar/N_2$, such as the different extent of gas losses experienced by the replicates during handling. The CI of the regression line and the estimated $\delta O_2/N_2$ can certainly benefit from improved analytical precision in the future.

To investigate how large analytical uncertainties could potentially affect the estimate of $\delta O_2/N_2$, we used a "York Fit" algorithm that takes into account the inherent uncertainty in both the independent ($\delta Ar/N_2$) and dependent ($\delta O_2/N_2$) variables in a generalized linear model (MATLAB code available at www.mathworks.com/matlabcentral/fileexchange/26586-linear-regression-with-errors-in-x-and-y) (*58*). We chose the pooled SD to represent the uncertainty associated with $\delta Ar/N_2$ and $\delta O_2/N_2$ data. The results are shown in fig. S6. In all three intervals (post-MPT, MPT, and pre-MPT), the York Fit yields a steeper slope, but none is significantly different from the slope yielded by the ordinary least squares (OLS) regression method used in our analysis. For the post-MPT samples, the York Fit slope is 2.16 ± 0.84 (2σ; same as below) with a *y* intercept of 1.9 ± 5.9‰, compared to the slope of 1.74 ± 0.44 and the *y* intercept of −0.9 ± 3.1‰ yielded by the OLS regression. For the MPT samples, the York Fit slope and *y* intercept are 2.31 ± 1.40 and 7.4 ± 10.6‰, respectively, while the OLS regression slope and *y* intercept are 1.60 ± 0.50 and 2.2 ± 3.8‰, respectively. The MPT samples have the largest departure of York Fit from the OLS fit. Last, for the pre-MPT samples, a slope of 1.77 ± 1.00 and a *y* intercept of 3.9 ± 7.5‰ are obtained from the York Fit, whereas the OLS slope and *y* intercept are 1.51 ± 0.38 and 2.0 ± 2.9‰, respectively.

Despite the changes to the slope when analytical uncertainties are taken into account, the estimated $\delta O_2/N_2$ when $\delta Ar/N_2$ is normalized to −7.1‰ does not change much (table S1), visually represented by the two types of regression lines intersecting near $\delta Ar/N_2 = -7.1$‰ (fig. S6). The corrected $\delta O_2/N_2$ (± 2σ) from York Fit is −13.47 ± 1.68, −8.96 ± 1.04, and −8.69 ± 1.06 for post-MPT, MPT, and pre-MPT samples, respectively. These results are very close to the OLS estimates made in the main text (table S1), because the value of −7.1‰ (the mean of all $\delta Ar/N_2$ values) is very close to the mean values of $\delta Ar/N_2$ in each age group. Visually, the York Fit tilts the slope of OLS regression around the arithmetic mean of the independent variables ($\delta Ar/N_2$). The estimated $\delta O_2/N_2$ near the arithmetic mean of $\delta Ar/N_2$ is therefore not substantially changed, but extrapolating $\delta O_2/N_2$ to $\delta Ar/N_2 = 0$ would lead to large differences (table S1). For these reasons, we still chose to regress $\delta O_2/N_2$ to $\delta Ar/N_2 = -7.1$‰ using the OLS method while acknowledging its inadequacy in addressing uncertainties in the variables. This facilitates the comparison of our regression results with the slopes of earlier work, all of which were done using the OLS method without factoring in the uncertainties in $\delta O_2/N_2$ or $\delta Ar/N_2$.

Data quality and rejection criteria

There are three batches of $\delta O_2/N_2$ and $\delta Ar/N_2$ dataset measured on ice collected from the Allan Hills BIA. The first batch was measured in 2013–2014 on samples drilled in 2010–2011 Antarctic field season. This batch of data ("batch 1") was first reported by Higgins *et al.* (*53*) with the method described by Dreyfus *et al.* (*54*). The second batch was measured in 2017 on samples collected in 2015–2016 Antarctic field season, with an updated gas extraction method described in this study. This batch of data ("batch 2") has been reported by Yan *et al.* (*19*). The third and final batch ("batch 3") was measured in 2018 and 2019, again with the updated method and on samples drilled in 2015–2016. This study presents the batch 3 data for the first time.

The key procedural distinction of batch 2 and 3 samples from batch 1 samples is that the pumping time has been greatly reduced. In batch 1 protocols, ice samples were pumped for an indefinite and variable amount of time until a vacuum level of 0.7 mtorr was reached. Each sample may therefore have experienced a varying degree of gas losses associated with storage and handling. The reduced pumping time applied to batch 2 and 3 data was intended to minimize gas losses due to pumping under vacuum and, if the losses are inevitable, to at least make the fractionation due to gas losses during pumping as consistent as possible. Note that this reduced pumping time does not prevent gas losses during storage and through fractures (if present).

In addition to analytical procedures, the conditions under which batch 1 to 3 samples are stored are also different. Specifically, batch 1 data were obtained from ice samples stored at a −25°C freezer for more than 2 years, and certain samples have visible internal fractures. In contrast, the $\delta O_2/N_2$ and $\delta Ar/N_2$ data reported in the present study come exclusively from ice cores drilled in the 2015–2016 field season. They have been stored at −36°C in the National Ice Core Facility in Denver, CO until retrieval for cutting and processing shortly before laboratory analyses and have no surface cracks or fractures. These storage and procedural differences may help explain the larger scatter observed in the $\delta O_2/N_2$-$\delta Ar/N_2$ data reported by Higgins *et al.* (*53*) made on samples dating back to the MPT (fig. S7). Batch 1 data were therefore excluded from our analysis (though we still present them in data S2, marked as batch 1). Batch 2 and 3 data are considered equivalent in terms of the data quality.

One post-MPT sample was rejected from batches 2 and 3 because of its very negative $\delta Ar/N_2$ value (−15.8‰). The $\delta O_2/N_2$ associated with this sample is −26.3‰, substantially (>5‰) more negative than typical ice core values. These anomalous negative ratios may arise from considerable gas loss experienced by this particular sample that greatly depletes Ar and O_2 relative to N_2. Six additional post-MPT samples were rejected because they are bracketed by pre-MPT age bins and might represent a different time slice than the shallow post-MPT samples. We still list these samples in data S2 but mark them as "anomalous gas loss" and "stratigraphy," respectively. Including these data points in the regression analysis does not change the conclusion of this paper.

In addition to gas losses, aerobic respiration and abiotic oxidation could affect the molecular oxygen concentrations in the trapped air. Even if O_2 consumption does not occur in situ inside the ice being measured, the large O_2 gradient could potentially drive a diffusive flux and modify the ice core $\delta O_2/N_2$. Many 2.0-Ma and all 2.7-Ma samples come from the sections are affected by respiration, evidenced by the depleted $\delta^{13}C$ values and anomalously elevated CO_2 levels (*19*). Thirteen $\delta O_2/N_2$ samples in batches 2 and 3, including one that had already been excluded, were rejected on this basis (labeled "respiration" in data S2). There are only four 2.0-Ma samples that are considered "pristine" (i.e., not affected by respiration). These four pristine $\delta O_2/N_2$-$\delta Ar/N_2$ data points fall within the envelop defined by the rest of the Allan Hills blue ice $\delta O_2/N_2$-$\delta Ar/N_2$ data, but they were excluded from inferring Early-Pleistocene PO_2 levels because of the small number of samples (annotated "2 Ma samples" in data S2). O_2 consumption by nonmicrobial redox reactions such as Fe(II) oxidation has been observed in the nearby (~500 km) Talos Dome ice core (*59*). In the case of Allan Hills samples, this process is expected to generate negligible impact on $\delta O_2/N_2$, because of

the low dust loading in the vicinity of Allan Hills [<700 parts per billion (ppb) during glacial and <15 ppb during interglacial periods] (*60*) and the low concentration of iron in the aeolian dust (~3% by mass).

In the case of very old ice here, an additional concern is the molecular diffusion through the ice that is capable of smoothing the signals in the gas record even after gases have become fully locked-in (*61*). This concern was partly motivated by the reduced variability observed in the portion of ALHIC1502 gas records below 150 m (fig. S2) and has been addressed in greater length by Yan *et al.* (*19*). We note that the variability reduction of $\delta^{18}O_{atm}$ bears some resemblance to the reduced variability of $\delta^{18}O_{atm}$ (among other properties) in the basal EDC ice below 3200 m (*62*). In the basal EDC record, the homogenization of dissolved impurities profile was hypothesized to arise from "accelerated migration re-crystallization, which results in spatial chemical sorting of the impurities" (*62*) under ice temperature close to the pressure melting point. The lack of $\delta^{18}O_{atm}$ variability between 3200 and 3260 m in EDC was not entirely understood, however, because if mechanical modification (stretching and annual layer thickening) was the reason, the 60-m layer would need to span an unlikely ~10 ka in time (*62*). An alternative possibility to stretching is diffusive smoothing, which has been shown to be capable of removing the submillennial-scale δD_{ice} variability (*63*) and would explain the lack of variability while preserving the mean values. It could be the case that the basal EDC δD_{ice} and $\delta^{18}O_{atm}$ have been subject to extensive diffusive smoothing and therefore lost its variability on multimeter length scale. If so, the extent of water isotope diffusion should be greater than that of gas diffusion (*61*). In the case of Allan Hills, calculations do not support the presence of molecular diffusion on the basis that δD of the ice shows considerable variability (*19*).

To summarize, all data measured on batch 1 samples and 23 data points from batches 2 and 3 were excluded. We retain a total number of 88 samples (each with at least one replicate) for calculations performed in this study.

SUPPLEMENTARY MATERIALS

Supplementary material for this article is available at https://science.org/doi/10.1126/sciadv.abj9341

REFERENCES AND NOTES

1. R. A. Berner, Phanerozoic atmospheric oxygen: New results using the GEOCARBSULF model. *Am. J. Sci.* **309**, 603–606 (2009).
2. P. G. Falkowski, M. E. Katz, A. J. Milligan, K. Fennel, B. S. Cramer, M. P. Aubry, R. A. Berner, M. J. Novacek, W. M. Zapol, The rise of oxygen over the past 205 million years and the evolution of large placental mammals. *Science* **309**, 2202–2204 (2005).
3. N. J. Shackleton, The carbon isotope record of the Cenozoic: History of organic carbon burial and of oxygen in the ocean and atmosphere. *Geol. Soc. Lond. Spec. Publ.* **26**, 423–434 (1987).
4. J. Farquhar, H. Bao, M. Thiemens, Atmospheric influence of Earth's earliest sulfur cycle. *Science* **289**, 756–758 (2000).
5. E. J. Bellefroid, A. V. S. Hood, P. F. Hoffman, M. D. Thomas, C. T. Reinhard, N. J. Planavsky, Constraints on Paleoproterozoic atmospheric oxygen levels. *Proc. Natl. Acad. Sci. U.S.A.* **115**, 8104–8109 (2018).
6. D. S. Hardisty, Z. Lu, N. J. Planavsky, A. Bekker, P. Philippot, X. Zhou, T. W. Lyons, An iodine record of paleoproterozoic surface ocean oxygenation. *Geology* **42**, 619–622 (2014).
7. I. J. Glasspool, A. C. Scott, Phanerozoic concentrations of atmospheric oxygen reconstructed from sedimentary charcoal. *Nat. Geosci.* **3**, 627–630 (2010).
8. D. A. Stolper, M. L. Bender, G. B. Dreyfus, Y. Yan, J. A. Higgins, A Pleistocene ice core record of atmospheric O_2 concentrations. *Science* **353**, 1427–1430 (2016).
9. R. A. Berner, G. P. Landis, Gas bubbles in fossil amber as possible indicators of the major gas composition of ancient air. *Science* **239**, 1406–1409 (1988).
10. N. J. Blamey, U. Brand, J. Parnell, N. Spear, C. Lécuyer, K. Benison, F. Meng, P. Ni, Paradigm shift in determining Neoproterozoic atmospheric oxygen. *Geology* **44**, 651–654 (2016).
11. L. Y. Yeung, Low oxygen and argon in the Neoproterozoic atmosphere at 815 Ma. *Earth Planet. Sci. Lett.* **480**, 66–74 (2017).
12. T. Sowers, M. Bender, D. Raynaud, Elemental and isotopic composition of occluded O_2 and N_2 in polar ice. *J. Geophys. Res. Atmos.* **94**, 5137–5150 (1989).
13. M. Bender, T. Sowers, V. Lipenkov, On the concentrations of O_2, N_2, and Ar in trapped gases from ice cores. *J. Geophys. Res. Atmos.* **100**, 18651–18660 (1995).
14. A. Landais, G. Dreyfus, E. Capron, K. Pol, M.-F. Loutre, D. Raynaud, V. Y. Lipenkov, L. Arnaud, V. Masson-Delmotte, D. Paillard, Towards orbital dating of the EPICA Dome C ice core using $\delta O_2/N_2$. *Clim. Past* **8**, 191–203 (2012).
15. T. Extier, A. Landais, C. Bréant, F. Prié, L. Bazin, G. Dreyfus, D. M. Roche, M. Leuenberger, On the use of $\delta^{18}O_{atm}$ for ice core dating. *Quat. Sci. Rev.* **185**, 244–257 (2018).
16. R. A. Berner, Geological nitrogen cycle and atmospheric N_2 over Phanerozoic time. *Geology* **34**, 413–415 (2006).
17. F. Herman, J.-D. Champagnac, Plio-Pleistocene increase of erosion rates in mountain belts in response to climate change. *Terra Nova* **28**, 2–10 (2016).
18. M. Kölling, I. Bouimetarhan, M. W. Bowles, T. Felis, T. Goldhammer, K.-U. Hinrichs, M. Schulz, M. Zabel, Consistent CO_2 release by pyrite oxidation on continental shelves prior to glacial terminations. *Nat. Geosci.* **12**, 929–934 (2019).
19. Y. Yan, M. L. Bender, E. J. Brook, H. M. Clifford, P. C. Kemeny, A. V. Kurbatov, S. Mackay, P. A. Mayewski, J. Ng, J. P. Severinghaus, J. A. Higgins, Two-million-year-old snapshots of atmospheric gases from Antarctic ice. *Nature* **574**, 663–666 (2019).
20. I. M. Whillans, W. A. Cassidy, Catch a falling star: Meteorites and old ice. *Science* **222**, 55–57 (1983).
21. M. L. Bender, B. Barnett, G. Dreyfus, J. Jouzel, D. Porcelli, The contemporary degassing rate of ^{40}Ar from the solid Earth. *Proc. Natl. Acad. Sci. U.S.A.* **105**, 8232–8237 (2008).
22. T. Kobashi, T. Ikeda-Fukazawa, M. Suwa, J. Schwander, T. Kameda, J. Lundin, A. Hori, H. Motoyama, M. Döring, M. Leuenberger, Post-bubble close-off fractionation of gases in polar firn and ice cores: Effects of accumulation rate on permeation through overloading pressure. *Atmos. Chem. Phys.* **15**, 13895–13914 (2015).
23. J. P. Severinghaus, R. Beaudette, M. A. Headly, K. Taylor, E. J. Brook, Oxygen-18 of O_2 records the impact of abrupt climate change on the terrestrial biosphere. *Science* **324**, 1431–1434 (2009).
24. M. L. Bender, Orbital tuning chronology for the Vostok climate record supported by trapped gas composition. *Earth Planet. Sci. Lett.* **204**, 275–289 (2002).
25. M. Haeberli, D. Baggenstos, J. Schmitt, M. Grimmer, A. Michel, T. Kellerhals, H. Fischer, Snapshots of mean ocean temperature over the last 700 000 years using noble gases in the EPICA Dome C ice core. *Clim. Past* **17**, 843–867 (2021).
26. H. Craig, Y. Horibe, T. Sowers, Gravitational separation of gases and isotopes in polar ice caps. *Science* **242**, 1675–1678 (1988).
27. H. D. Holland, Volcanic gases, black smokers, and the Great Oxidation Event. *Geochim. Cosmochim. Acta* **66**, 3811–3826 (2002).
28. A. Jeltsch-Thömmes, G. Battaglia, O. Cartapanis, S. L. Jaccard, F. Joos, Low terrestrial carbon storage at the Last Glacial Maximum: Constraints from multi-proxy data. *Clim. Past* **15**, 849–879 (2019).
29. E. A. G. Schuur, A. D. McGuire, C. Schädel, G. Grosse, J. W. Harden, D. J. Hayes, G. Hugelius, C. D. Koven, P. Kuhry, D. M. Lawrence, S. M. Natali, D. Olefeldt, V. E. Romanovsky, K. Schaefer, M. R. Turetsky, C. C. Treat, J. E. Vonk, Climate change and the permafrost carbon feedback. *Nature* **520**, 171–179 (2015).
30. L. E. Lisiecki, M. E. Raymo, A Pliocene-Pleistocene stack of 57 globally distributed benthic $\delta^{18}O$ records. *Paleoceanography* **20**, PA1003 (2005).
31. P. U. Clark, D. Archer, D. Pollard, J. D. Blum, J. A. Rial, V. Brovkin, A. C. Mix, N. G. Pisias, M. Roy, The middle Pleistocene transition: Characteristics. Mechanisms, and implications for long-term changes in atmospheric pCO_2. *Quat. Sci. Rev.* **25**, 3150–3184 (2006).
32. C. J. Berends, P. Köhler, L. J. Lourens, R. S. W. van de Wal, On the cause of the mid-pleistocene transition. *Rev. Geophys.* **59**, e2020RG000727 (2021).
33. H. L. Ford, M. E. Raymo, Regional and global signals in seawater $\delta^{18}O$ records across the mid-Pleistocene transition. *Geology* **48**, 113–117 (2019).
34. E. J. Rohling, G. L. Foster, K. M. Grant, G. Marino, A. P. Roberts, M. E. Tamisiea, F. Williams, Sea-level and deep-sea-temperature variability over the past 5.3 million years. *Nature* **508**, 477–482 (2014).
35. J. Boellstorff, North American Pleistocene stages reconsidered in light of probable pliocene-pleistocene continental glaciation. *Science* **202**, 305–307 (1978).
36. J. Ehlers, P. L. Gibbard, The extent and chronology of Cenozoic global glaciation. *Quat. Int.* **164-165**, 6–20 (2007).
37. S. Sosdian, Y. Rosenthal, Deep-sea temperature and ice volume changes across the Pliocene-Pleistocene climate transitions. *Science* **325**, 306–310 (2009).
38. T. B. Chalk, M. P. Hain, G. L. Foster, E. J. Rohling, P. F. Sexton, M. P. S. Badger, S. G. Cherry, A. P. Hasenfratz, G. H. Haug, S. L. Jaccard, A. Martinez-Garcia, H. Palike, R. D. Pancost, P. A. Wilson, Causes of ice age intensification across the mid-Pleistocene transition. *Proc. Natl. Acad. Sci. U.S.A.* **114**, 13114–13119 (2017).

39. S. P. S. Gulick, J. M. Jaeger, A. C. Mix, H. Asahi, H. Bahlburg, C. L. Belanger, G. B. B. Berbel, L. Childress, E. Cowan, L. Drab, M. Forwick, A. Fukumura, S. Ge, S. Gupta, A. Kioka, S. Konno, L. J. Le Vay, C. März, K. M. Matsuzaki, E. L. Mc Clymont, C. Moy, J. Müller, A. Nakamura, T. Ojima, F. R. Ribeiro, K. D. Ridgway, O. E. Romero, A. L. Slagle, J. S. Stoner, G. St-Onge, I. Suto, M. D. Walczak, L. L. Worthington, I. Bailey, E. Enkelmann, R. Reece, J. M. Swartz, Mid-Pleistocene climate transition drives net mass loss from rapidly uplifting St. Elias Mountains, Alaska. *Proc. Natl. Acad. Sci. U.S.A.* **112**, 15042–15047 (2015).
40. M. A. Torres, N. Moosdorf, J. Hartmann, J. F. Adkins, A. J. West, Glacial weathering, sulfide oxidation, and global carbon cycle feedbacks. *Proc. Natl. Acad. Sci. U.S.A.* **114**, 8716–8721 (2017).
41. K. Horan, R. G. Hilton, D. Selby, C. J. Ottley, D. R. Gröcke, M. Hicks, K. W. Burton, Mountain glaciation drives rapid oxidation of rock-bound organic carbon. *Sci. Adv.* **3**, e1701107 (2017).
42. A. S. Colman, F. T. Mackenzie, H. D. Holland, P. Van Cappellen, E. D. Ingall, Redox stabilization of the atmosphere and oceans and marine productivity. *Science* **275**, 406–408 (1997).
43. J. R. Farmer, B. Hönisch, L. L. Haynes, D. Kroon, S. Jung, H. L. Ford, M. E. Raymo, M. Jaume-Seguí, D. B. Bell, S. L. Goldstein, L. D. Pena, M. Yehudai, J. Kim, Deep Atlantic Ocean carbon storage and the rise of 100,000-year glacial cycles. *Nat. Geosci.* **12**, 355–360 (2019).
44. A. Jeltsch-Thömmes, F. Joos, Modeling the evolution of pulse-like perturbations in atmospheric carbon and carbon isotopes: The role of weathering–sedimentation imbalances. *Clim. Past* **16**, 423–451 (2020).
45. L. D. Pena, S. L. Goldstein, Thermohaline circulation crisis and impacts during the mid-Pleistocene transition. *Science* **345**, 318–322 (2014).
46. G. Delisle, J. Sievers, Sub-Ice topography and meteorite finds near the Allan Hills and the near Western Ice Field, Victoria Land, Antarctica. *J. Geophys. Res. Planet.* **96**, 15577–15587 (1991).
47. L. Schultz, J. O. Annexstad, G. Delisle, Ice movement and mass balance at the Allan Hills Icefield. *Antarct. J. US* **25**, 94–95 (1990).
48. N. E. Spaulding, V. B. Spikes, G. S. Hamilton, P. A. Mayewski, N. W. Dunbar, R. P. Harvey, J. Schutt, A. V. Kurbatov, Ice motion and mass balance at the Allan Hills blue-ice area, Antarctica, with implications for paleoclimate reconstructions. *J. Glaciol.* **58**, 399–406 (2012).
49. R. Dadic, M. Schneebeli, N. A. N. Bertler, M. Schwikowski, M. Matzl, Extreme snow metamorphism in the Allan Hills, Antarctica, as an analogue for glacial conditions with implications for stable isotope composition. *J. Glaciol.* **61**, 1171–1182 (2015).
50. R. Bintanja, On the glaciological, meteorological, and climatological significance of Antarctic blue ice areas. *Rev. Geophys.* **37**, 337–359 (1999).
51. L. Kehrl, H. Conway, N. Holschuh, S. Campbell, A. V. Kurbatov, N. E. Spaulding, Evaluating the duration and continuity of potential climate records from the Allan Hills Blue Ice Area, East Antarctica. *Geophys. Res. Lett.* **45**, 4096–4104 (2018).
52. J. A. Menking, E. J. Brook, S. A. Shackleton, J. P. Severinghaus, M. N. Dyonisius, V. Petrenko, J. R. McConnell, R. H. Rhodes, T. K. Bauska, D. Baggenstos, Spatial pattern of accumulation at Taylor Dome during Marine Isotope Stage 4: Stratigraphic constraints from Taylor Glacier. *Clim. Past* **15**, 1537–1556 (2019).
53. J. A. Higgins, A. V. Kurbatov, N. E. Spaulding, E. Brook, D. S. Introne, L. M. Chimiak, Y. Z. Yan, P. A. Mayewski, M. L. Bender, Atmospheric composition 1 million years ago from blue ice in the Allan Hills, Antarctica. *Proc. Natl. Acad. Sci. U.S.A.* **112**, 6887–6891 (2015).
54. G. B. Dreyfus, F. Parrenin, B. Lemieux-Dudon, G. Durand, V. Masson-Delmotte, J. Jouzel, J. M. Barnola, L. Panno, R. Spahni, A. Tisserand, U. Siegenthaler, M. Leuenberger, Anomalous flow below 2700 m in the EPICA Dome C ice core detected using $\delta^{18}O$ of atmospheric oxygen measurements. *Clim. Past* **3**, 341–353 (2007).
55. S. Emerson, P. D. Quay, C. Stump, D. Wilbur, R. Schudlich, Chemical tracers of productivity and respiration in the subtropical Pacific Ocean. *J. Geophys. Res. Oceans* **100**, 15873–15887 (1995).
56. K. Kawamura, F. Parrenin, L. Lisiecki, R. Uemura, F. Vimeux, J. P. Severinghaus, M. A. Hutterli, T. Nakazawa, S. Aoki, J. Jouzel, M. E. Raymo, K. Matsumoto, H. Nakata, H. Motoyama, S. Fujita, K. Goto-Azuma, Y. Fujii, O. Watanabe, Northern Hemisphere forcing of climatic cycles in Antarctica over the past 360,000 years. *Nature* **448**, 912–916 (2007).
57. M. Suwa, M. L. Bender, Chronology of the Vostok ice core constrained by O_2/N_2 ratios of occluded air, and its implication for the Vostok climate records. *Quat. Sci. Rev.* **27**, 1093–1106 (2008).
58. D. York, N. M. Evensen, M. L. Martınez, J. De Basabe Delgado, Unified equations for the slope, intercept, and standard errors of the best straight line. *Am. J. Phys.* **72**, 367–375 (2004).
59. G. Baccolo, B. Delmonte, P. B. Niles, G. Cibin, E. D. Stefano, D. Hampai, L. Keller, V. Maggi, A. Marcelli, J. Michalski, C. Snead, M. Frezzotti, Jarosite formation in deep Antarctic ice provides a window into acidic, water-limited weathering on Mars. *Nat. Commun.* **12**, 436 (2021).
60. S. M. Aarons, S. M. Aciego, P. Gabrielli, B. Delmonte, J. M. Koornneef, A. Wegner, M. A. Blakowski, The impact of glacier retreat from the Ross Sea on local climate: Characterization of mineral dust in the Taylor Dome ice core, East Antarctica. *Earth Planet. Sci. Lett.* **444**, 34–44 (2016).
61. B. Bereiter, H. Fischer, J. Schwander, T. F. Stocker, Diffusive equilibration of N_2, O_2 and CO_2 mixing ratios in a 1.5-million-years-old ice core. *The Cryosphere* **8**, 245–256 (2014).
62. J.-L. Tison, M. de Angelis, G. Littot, E. Wolff, H. Fischer, M. Hansson, M. Bigler, R. Udisti, A. Wegner, J. Jouzel, B. Stenni, S. Johnsen, V. Masson-Delmotte, A. Landais, V. Lipenkov, L. Loulergue, J.-M. Barnola, J.-R. Petit, B. Delmonte, G. Dreyfus, D. Dahl-Jensen, G. Durand, B. Bereiter, A. Schilt, R. Spahni, K. Pol, R. Lorrain, R. Souchez, D. Samyn, Retrieving the paleoclimatic signal from the deeper part of the EPICA Dome C ice core. *The Cryosphere* **9**, 1633–1648 (2015).
63. K. Pol, V. Masson-Delmotte, S. Johnsen, M. Bigler, O. Cattani, G. Durand, S. Falourd, J. Jouzel, B. Minster, F. Parrenin, C. Ritz, H. C. Steen-Larsen, B. Stenni, New MIS 19 EPICA Dome C high resolution deuterium data: Hints for a problematic preservation of climate variability at sub-millennial scale in the "oldest ice". *Earth Planet. Sci. Lett.* **298**, 95–103 (2010).
64. J. R. Petit, J. Jouzel, D. Raynaud, N. I. Barkov, J. M. Barnola, I. Basile, M. Bender, J. Chappellaz, M. Davis, G. Delaygue, M. Delmotte, V. M. Kotlyakov, M. Legrand, V. Y. Lipenkov, C. Lorius, L. Pepin, C. Ritz, E. Saltzman, M. Stievenard, Climate and atmospheric history of the past 420,000 years from the Vostok ice core, Antarctica. *Nature* **399**, 429–436 (1999).
65. U. Siegenthaler, T. F. Stocker, E. Monnin, D. Luthi, J. Schwander, B. Stauffer, D. Raynaud, J. M. Barnola, H. Fischer, V. Masson-Delmotte, J. Jouzel, Stable carbon cycle-climate relationship during the late Pleistocene. *Science* **310**, 1313–1317 (2005).
66. D. Lüthi, M. Le Floch, B. Bereiter, T. Blunier, J. M. Barnola, U. Siegenthaler, D. Raynaud, J. Jouzel, H. Fischer, K. Kawamura, T. F. Stocker, High-resolution carbon dioxide concentration record 650,000-800,000 years before present. *Nature* **453**, 379–382 (2008).
67. B. Bereiter, S. Eggleston, J. Schmitt, C. Nehrbass-Ahles, T. F. Stocker, H. Fischer, S. Kipfstuhl, J. Chappellaz, Revision of the EPICA Dome C CO_2 record from 800 to 600 kyr before present. *Geophys. Res. Lett.* **42**, 542–549 (2015).
68. J. P. Severinghaus, A. Grachev, M. Battle, Thermal fractionation of air in polar firn by seasonal temperature gradients. *Geochem. Geophys. Geosyst.* **2**, 2000GC000146 (2001).
69. J. P. Severinghaus, M. O. Battle, Fractionation of gases in polar ice during bubble close-off: New constraints from firn air Ne, Kr and Xe observations. *J. Geophys. Res. Earth Surface* **244**, 474–500 (2006).
70. M. M. Herron, C. C. Langway, Firn densification: An empirical model. *J. Glaciol.* **25**, 373–385 (1980).
71. C. Huber, U. Beyerle, M. Leuenberger, J. Schwander, R. Kipfer, R. Spahni, J. P. Severinghaus, K. Weiler, Evidence for molecular size dependent gas fractionation in firn air derived from noble gases, oxygen, and nitrogen measurements. *Earth Planet. Sci. Lett.* **243**, 61–73 (2006).
72. M. O. Battle, J. P. Severinghaus, E. D. Sofen, D. Plotkin, A. J. Orsi, M. Aydin, S. A. Montzka, T. Sowers, P. P. Tans, Controls on the movement and composition of firn air at the West Antarctic Ice Sheet Divide. *Atmos. Chem. Phys.* **11**, 11007–11021 (2011).
73. S. Fujita, J. Okuyama, A. Hori, T. Hondoh, Metamorphism of stratified firn at Dome Fuji, Antarctica: A mechanism for local insolation modulation of gas transport conditions during bubble close off. *J. Geophys. Res. Earth Surface* **114**, F03023 (2009).
74. A. Landais, J. Chappellaz, M. Delmotte, J. Jouzel, T. Blunier, C. Bourg, N. Caillon, S. Cherrier, B. Malaizé, V. Masson-Delmotte, D. Raynaud, J. Schwander, J. P. Steffensen, A tentative reconstruction of the last interglacial and glacial inception in Greenland based on new gas measurements in the Greenland Ice Core Project (GRIP) ice core. *J. Geophys. Res. Atmos.* **108**, 4563 (2003).
75. T. Ikeda-Fukazawa, K. Fukumizu, K. Kawamura, S. Aoki, T. Nakazawa, T. Hondoh, Effects of molecular diffusion on trapped gas composition in polar ice cores. *Earth Planet. Sci. Lett.* **229**, 183–192 (2005).
76. B. Bereiter, J. Schwander, D. Lüthi, T. F. Stocker, Change in CO_2 concentration and O_2/N_2 ratio in ice cores due to molecular diffusion. *Geophys. Res. Lett.* **36**, L05703 (2009).
77. K. S. Johnson, M. B. Bif, Constraint on net primary productivity of the global ocean by Argo oxygen measurements. *Nat. Geosci.* **14**, 769–774 (2021).
78. M. E. Galvez, Redox constraints on a Cenozoic imbalance in the organic carbon cycle. *Am. J. Sci.* **320**, 730–751 (2020).
79. J. C. Walker, Stability of atmospheric oxygen. *Am. J. Sci.* **274**, 193–214 (1974).

Acknowledgments: We thank the U.S. Ice Drilling Design and Operations (IDDO), M. Waszkiewicz, P. Kemeny, S. Mackay, and K. Borek Air for assistance with the field work. We also thank R. Nunn and G. Hargreaves at the National Science Foundation Ice Core Facility for help with ice core sample processing and archiving. Geospatial support for this work was provided by the Polar Geospatial Center under NSF-OPP awards 1043681 and 1559691. Discussion with M. Bender greatly improved the manuscript. The authors are grateful to three anonymous reviewers for their constructive comments. **Funding:** This work was supported by the Rice University Poh-Hsi Pan Postdoctoral Fellowship (to Y.Y.) and the NSF (grant

ANT-1443263 to J.A.H., grant ANT-1443276 to E.J.B., grant ANT-1443306 to A.V.K., grant NSF-0538630 to J.P.S., and grant ANT-0944343 to J.P.S.) **Author contributions:** Conceptualization: Y.Y. and J.A.H. Methodology: Y.Y. and J.A.H. Investigation: Y.Y. and J.A.H. Visualization: Y.Y. Supervision: J.A.H., J.P.S., E.J.B., and A.V.K. Writing—original draft: Y.Y. and J.A.H. Writing—review and editing: A.V.K., E.J.B., and J.P.S. **Competing interests:** The authors declare that they have no competing interests. **Data and materials availability:** All data needed to evaluate the conclusions in the paper are present in the paper and/or the Supplementary Materials. Gas ratio and isotope data used in this study are available in the Supplementary Materials (data S1 and S2). They are also available at the U.S. Antarctic Program Data Center with the following digital object identifiers (DOIs): 10.15784/601201 ($^{40}Ar_{atm}$) and 10.15784/601483 (O_2/N_2/Ar elemental and isotopic ratios).

Submitted 10 June 2021
Accepted 3 November 2021
Published 15 December 2021
10.1126/sciadv.abj9341

ScienceAdvances

Ice core evidence for atmospheric oxygen decline since the Mid-Pleistocene transition

Yuzhen YanEdward J. BrookAndrei V. KurbatovJeffrey P. SeveringhausJohn A. Higgins

Sci. Adv., 7 (51), eabj9341. • DOI: 10.1126/sciadv.abj9341